Mechanical properties of atomically thin boron nitride and the role of interlayer interactions

Mechanical Properties of Atomically Thin Boron Nitride and the Role of Interlayer Interactions

Aleksey Falin,[1] Qiran Cai,[1] Elton J. G. Santos,[2,3] Declan Scullion,[2] Dong Qian,[4] Rui Zhang,[4,5] Zhi Yang,[6] Shaoming Huang,[6] Kenji Watanabe,[7] Takashi Taniguchi,[7] Matthew R. Barnett,[1] Ying Chen,[1] Rodney S. Ruoff[8,9,10] and Lu Hua Li[1]**

1. Institute for Frontier Materials, Deakin University, Geelong Waurn Ponds Campus, VIC 3216, Australia

2. School of Mathematics and Physics, Queen's University Belfast, BT7 1NN, United Kingdom

3. School of Chemistry and Chemical Engineering, Queen's University Belfast, BT9 5AL, United Kingdom

4. Department of Mechanical Engineering, The University of Texas at Dallas, Richardson, TX 75080, USA

5. School of Astronautics, Northwestern Polytechnical University, Xi'an 710072, China

6. Nanomaterials and Chemistry Key Laboratory, Wenzhou University, 276 Xueyuan Middle Road, Wenzhou, Zhejiang 325027, China

7. National Institute for Materials Science, Namiki 1-1, Tsukuba, Ibaraki 305-0044, Japan

8. Center for Multidimensional Carbon Materials, Institute for Basic Science (IBS), Ulsan 44919, Republic of Korea

9. Department of Chemistry, Ulsan National Institute of Science and Technology (UNIST), Ulsan 44919, Republic of Korea

10. School of Materials Science and Engineering, Ulsan National Institute of Science and Technology (UNIST), Ulsan 44919, Republic of Korea

Abstract

Atomically thin boron nitride (BN) nanosheets are important two-dimensional nanomaterials with many unique properties distinct from those of graphene. However, the lack of the knowledge of their intrinsic mechanical properties greatly hindered their applications. Herein, we experimentally address this problem for the first time by testing high-quality single-crystalline mono- and few-layer BN nanosheets. The results of indentation tests using atomic force microscopy show that BN nanosheets are one of the strongest electrically insulating materials. More intriguingly, few-layer BN shows mechanical behaviors quite different from those of few-layer graphene. In striking contrast to graphene, whose strength decreases by more than 30% when the number of layers increases from 1 to 8, the mechanical strength of BN nanosheets is not sensitive to increasing thickness. We attribute this difference to the distinct interlayer interactions in these two materials: graphene layers experience spontaneous interlayer sliding under load, resulting in stress concentration in the bottom layers; on the other hand, BN layers firmly attach to each other, so stress is homogeneously distributed among them under similar conditions. The significantly better mechanical integrity of BN nanosheets makes them a more attractive candidate than graphene for several applications, *e.g.* as mechanical reinforcements.

Two-dimensional (2D) nanomaterials, such as graphene, boron nitride (BN), and molybdenum disulfide (MoS_2) nanosheets have many fascinating properties that could be useful for a wide range of applications, such as composite, nanoelectromechanical systems (NEMS), and sensing. Investigations on the mechanical properties of these nanomaterials are, therefore, essential. In this regard, the mechanical properties of monolayer (1L) graphene have been systematically studied. Although the reported experimental values of the elastic modulus of high-quality graphene vary between 0.5 and 2.4 TPa,[1-5] most studies obtained a value of ~1 TPa, *i.e.* an effective Young's modulus (E^{2D}) of 342 N/m with an effective thickness of 0.335 nm, consistent with many theoretical calculations.[6-10] The theoretical and experimental fracture strengths of graphene are in the range of 70–130 GPa, and the intrinsic strain is between 14% and 33%.[1,7-11] It has been found that although low levels of defects do not have a negative influence on the elastic modulus of graphene,[12-14] their presence can greatly deteriorate its strength.[12,15-18] The effect of grain boundaries in graphene has also been studied theoretically and experimentally.[11,19-22] As for the mechanical properties of few-layer graphene, it has been found that both the Young's modulus and strength of graphene decrease with increased thickness.[23-30] This has been explained by strong in-plane covalent bonding bonds and weak van der Waals interactions between the layers.[28,31-33] The intrinsic mechanical properties of many other 2D nanomaterials, including MoS_2, tungsten disulfide (WS_2), and phosphorene have also been studied.[34-37]

BN nanosheets, which are composed of atomically thin hexagonal boron nitride (hBN), have a structure similar to graphene but possess many distinguished properties.[38] They, sometimes called white graphene, are insulators with bandgaps close to 6 eV. BN nanosheets are excellent

dielectric substrates for graphene, MoS_2, and other 2D nanomaterials.[39,40] In addition, BN nanosheets are efficient emitters of deep ultraviolet light.[41,42] Moreover, monolayer BN is stable up to 800 °C in air;[43] in contrast, graphene starts to oxidize at 300 °C under the same conditions.[44] Therefore, BN nanosheets are excellent candidates for reinforcing ceramic and metal matrix composites, which are normally fabricated at high temperatures. BN nanosheets can also be used in polymer composites when electrical insulation, optical transparency, and enhanced thermal stability are desired. The thermal and chemical inertness of BN nanosheets are also ideal for corrosion protection at high temperatures.[45,46] In addition, BN nanosheets provide high sensitivity and reusability in sensing applications.[47-51]

There have been a few measurements on few-layer BN produced by chemical vapor deposition (CVD), but the mechanical properties of monolayer BN have never been experimentally examined. Song *et al.* first reported that the elastic modulus of CVD-grown bilayer BN nanosheets was 0.334 ± 0.024 TPa (*i.e.* E^{2D} = 112 ± 8 N/m), and their fracture strength was 26.3 GPa (*i.e.* 8.8 N/m).[52] These values are much smaller than those predicted by theoretical calculations. From the aspect of theoretical calculations, although the mechanical properties of few-layer BN have never been theoretically investigated, the Young's modulus of 1L BN was predicted to be 0.716–0.977 TPa (*i.e.* E^{2D} = 239–326 N/m with an effective thickness of 0.334 nm), while its breaking strength fell in the wide range of 68–215 GPa (*i.e.* 23–72 N/m).[52-60] The degraded mechanical properties of the 2L CVD BN reported by Song *et al.* were attributed to the presence of defects and grain boundaries.[61,62] Kim *et al.* measured the Young's modulus of ~15 nm-thick (i.e. ~45L) BN nanosheets produced by CVD to be 1.16 ± 0.1 TPa.[63] Li *et al.* investigated the bending modulus of ~50 nm-thick (*i.e.* ~150L) BN nanosheets.[64] The lack of

systematic study of the intrinsic mechanical properties of atomically thin BN of different thicknesses greatly hinders the study and use of these novel nanomaterials.

Here, the intrinsic mechanical properties of mono- and few-layer BN are experimentally revealed for the first time. The high-quality monolayer BN is found to have a Young's modulus of 0.865 ± 0.073 TPa, and fracture strength of 70.5 ± 5.5 GPa. In contrast to graphene, whose strength decreases dramatically with an increase in thickness, few-layer BN nanosheets (at least up to 9L) have a strength similar to that of 1L BN. Detailed theoretical and experimental investigations indicate that the difference is caused by the distinct interlayer interactions in these two nanomaterials under large in-plane strain and out-of-plane compression. This study suggests that BN nanosheets are one of the strongest insulating materials, and more importantly, the strong interlayer interaction in BN nanosheets, along with their excellent thermal stability, make them ideal for mechanical reinforcement applications.

Results

The BN nanosheets were mechanically exfoliated from high-quality hBN single crystals[65] on 90 nm-thick silicon oxide covered silicon (SiO_2/Si) substrates with pre-fabricated micro-wells of 650 nm in radius. Figure 1a shows the optical microscopy image of a 1L BN covering 7 micro-wells, and the corresponding atomic force microscopy (AFM) image is displayed in Figure 1b. According to the height trace, the thickness of the 1L BN was 0.48 nm (Figure 1c). The thickness of 2L and 3L BN was about 0.85 and 1.02 nm, respectively (see Supplementary Information, Figure S1). Figure 1d shows the Raman spectrum of the suspended part of the 1L BN, and its G band frequency centered at 1366.5 cm^{-1}, which is very close to that of bulk hBN (i.e. 1366.4 cm^{-}

[1]). For comparison purposes, mono- and few-layer graphene were also produced following the same method (see Supplementary Information, Figure S2-3).

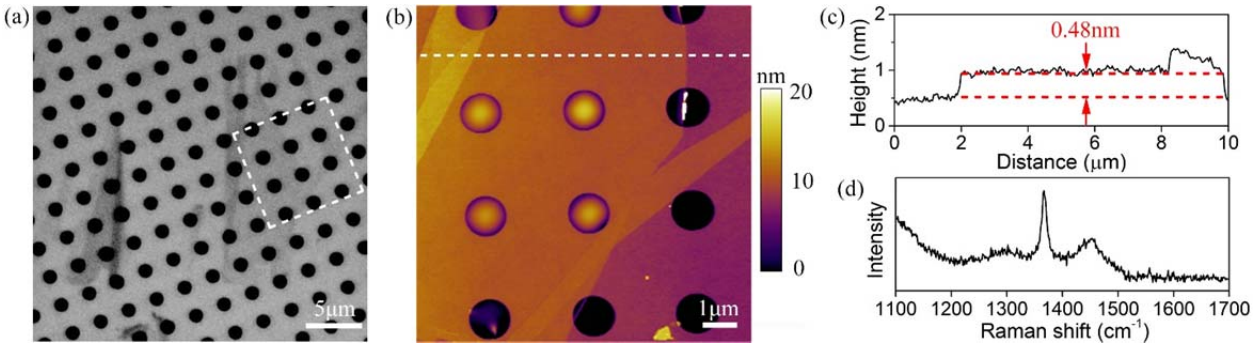

Figure.1 Characterization of 1L BN. (a) Optical microscopy image of a 1L BN on a SiO_2/Si substrate with micro-wells of 1.3 μm in diameter; (b) AFM image of the BN nanosheet marked in the square of (a); (c) the corresponding height trace of the dashed line in (b); (d) Raman spectrum of the suspended part of the 1L BN.

The mechanical properties of the mono- and few-layer graphene and BN nanosheets were studied by indentation at the center of the suspended regions using AFM. To obtain load-displacement curves, the AFM displacements were converted into the deflection (δ) of the nanosheets, as follows:

$$\delta = \Delta Z_{piezo} - \delta_{tip} \quad (1)$$

where δ_{tip} is the deflection of the AFM tip; ΔZ_{piezo} is the z displacement of the AFM piezo/sample.[4,66] The deflection of 2D nanomaterials during indentation can be divided into two regions. Under a relatively small uniaxial load, the isotropic elastic response of 2D nanomaterials is linear; when the load and deformation are large, the load-displacement relation becomes

cubic.[1,23] Therefore, the total load-displacement relationship in 2D nanomaterials during indentation includes both the linear and cubic terms:[1]

$$F = {\sigma_0}^{2D}(\pi a)\left(\frac{\delta}{a}\right) + E^{2D}(q^3 a)\left(\frac{\delta}{a}\right)^3 \qquad (2)$$

where F is the applied load; ${\sigma_0}^{2D}$ is the 2D pre-tension of the nanosheet; δ is the deflection of the nanosheet under load F; a is the radius of the micro-well; q=1/(1.049–0.15ν–0.16ν^2) is a dimensionless constant; and ν is Poisson's ratio. E^{2D} is the 2D effective Young's modulus of the nanosheet, which can be converted to the conventional bulk (*i.e.* volumetric) modulus (E) by dividing it by the thickness of the nanosheet.[67] For BN, we used an effective thickness of 0.334 nm, and a Poisson ratio of 0.211;[53,55] for graphene, the effective thickness was 0.335 nm, and the Poisson ratio was 0.165.[1] The elastic moduli of atomically thin BN and graphene could be deduced by fitting the loading curves using Eq. 2.[1,34,52] Typical loading curves of 1-3L graphene and BN nanosheets till a displacement of ~50 nm, and the corresponding fittings, are compared in Figure 2.

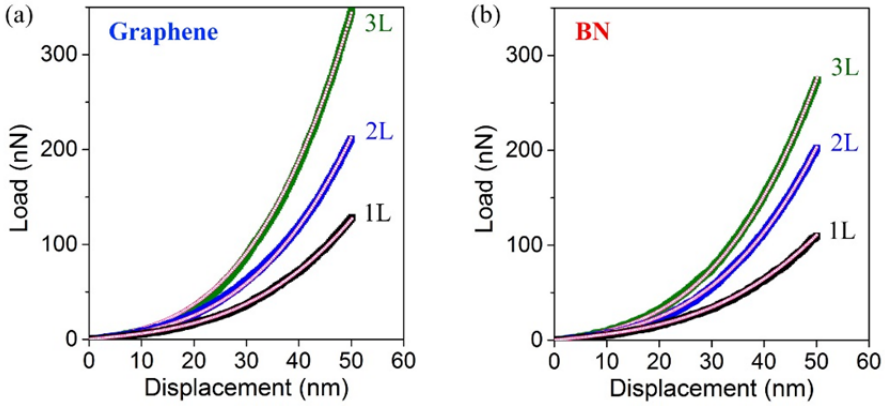

Figure 2. Load-displacement curves and the corresponding fittings of 1-3L (a) graphene and (b) BN nanosheets.

Figure 3 summarizes the Young's moduli of graphene and BN nanosheets of different thicknesses. The E^{2D} of 1-3L graphene were 342 ± 8 N·m^{-1} (N = 11), 645 ± 16 N·m^{-1} (N = 13) and 985 ± 10 N·m^{-1} (N = 6), respectively. These values are consistent with those obtained by previous studies using AFM.[1,23] The average E^{2D} of 1L BN was 289 ± 24 N·m^{-1} (N = 11). This result is in excellent agreement with a few theoretical predictions.[53-56,68] The E^{2D} of 2L and 3L BN nanosheets were 590 ± 38 (N = 14) and 822 ± 44 N·m^{-1} (N = 6), respectively. The dashed lines in Figure 3a show the projections of the E^{2D} of graphene and BN nanosheets with increased thickness, which were obtained by multiplying the E^{2D} values of their monolayers by the number of layers. In other words, the difference in the experimental data and dashed lines indicates the relative changes of E^{2D} with the increased thickness of graphene and BN. It can be seen that the E^{2D} of graphene deviated more than that of BN as thickness increased. This can be shown more clearly by plotting the (volumetric) Young's moduli of graphene and BN at different thicknesses (Figure 3b). The E of 1L graphene was 1.026 ± 0.022 TPa, but that of 8L graphene was reduced to 0.942 ± 0.003 TPa. The E values of 1L and 9L BN nanosheets were quite similar: 0.865 ± 0.073 and 0.856 ± 0.003 TPa, respectively.

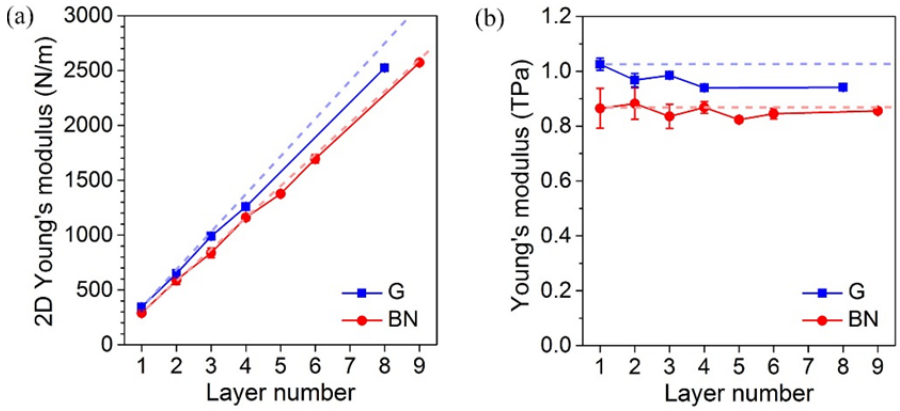

Figure 3. Elastic properties of graphene and BN nanosheets. (a) 2D Young's modulus (E^{2D}) of graphene (G) and BN nanosheets of different thicknesses, along with the dashed projections calculated based on multiplying of the number of layers by the E^{2D} of the monolayers; (b) Volumetric Young's modulus (E) of graphene and BN nanosheets of different thicknesses, along with dashed lines that show the Young's moduli of 1L graphene and BN.

The strengths of graphene and BN nanosheets of different thicknesses were calculated based on load-displacement curves and fracture loads using finite element simulation. The fracture loads (F_f) of graphene and BN of different thicknesses are shown in Figure 4a. Similar to Figure 3a, the dashed lines in Figure 4a are the projections calculated by multiplying the fracture load of 1L graphene and BN by the number of layers. The fracture loads of multilayer graphene deviated more from the blue dashed line as the thickness increased. For example, the fracture load of 8L graphene was 53.7% smaller than 8 times the fracture load of the 1L graphene. In contrast, the fracture loads of BN of different thicknesses closely followed the red dashed line. These different trends are also shown in their mechanical strengths. As shown in Figure 4b and c, the breaking strengths of graphene were 125.0 ± 0 GPa (i.e. 2D strength of 41.9 ± 0 $N \cdot m^{-1}$), 107.7 ± 4.3 GPa (72.1 ± 2.9 $N \cdot m^{-1}$), 105.6 ± 6.0 GPa (106.2 ± 6.0 $N \cdot m^{-1}$), and 85.3 ± 5.4 GPa (228.6 ± 14.5 $N \cdot m^{-1}$) for monolayer, bilayer, trilayer, and eight layers, respectively. Again, these values are in agreement with those reported previously.[23,28] According to these values, no defect was present in the part of graphene close to the indentation center.[11,12] The strengths of 1-3L BN were 70.5 ± 5.5 GPa (23.6 ± 1.8 $N \cdot m^{-1}$), 68.0 ± 6.8 GPa (45.4 ± 4.5 $N \cdot m^{-1}$), and 76.9 ± 2.3 GPa (77.0 ± 2.3 $N \cdot m^{-1}$), respectively. Previous theoretical calculations yielded a quite different breaking strength for 1L BN, and our experimental results match well the value calculated by Peng *et al.*

using DFT,[55] but are much smaller than the those predicted by Han *et al.* and Mortazavi *et al.*, both of which used molecular dynamics (MD) simulations.[53,59]

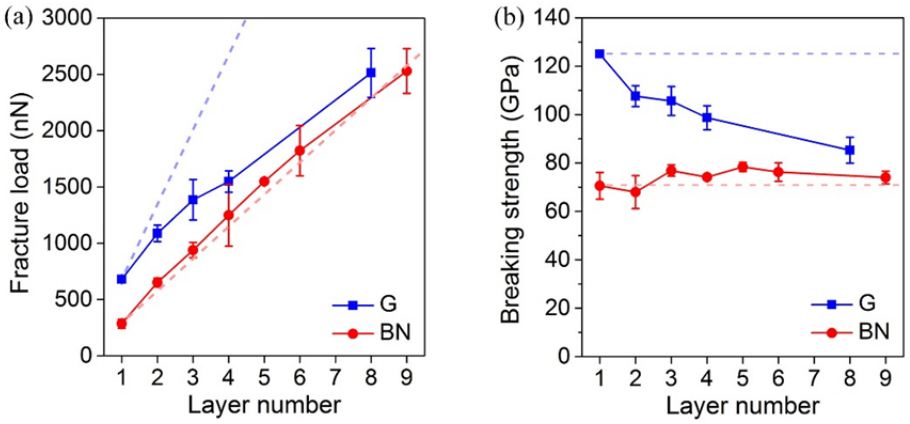

Figure 4. Mechanical strengths of graphene and BN nanosheets. (a) Fracture load and (b) breaking strength of graphene and BN of different thicknesses. The dashed lines in (a) are the projections of the fracture load of BN and graphene (G) of different thicknesses based on the multiplication of the strength of their monolayers by the number of layers.

The finite element simulations were also used to resolve the strain distribution in BN under a fracture load. Figure 5 shows the nominal strain distribution in a 1L BN. The maximum strain occurred at the very center of the load. That is, only a small portion of the BN under and adjacent to the indenter tip (dashed circle in Figure 5b) was highly strained, and the behavior of the rest of the nanosheet was almost linear elastic. This can be also seen from the strain distribution curve along the 650 nm radius of the suspended nanosheet (Figure 5c). The maximum nominal strain in this 1L BN was ~17%. Similarly to the trend of the strength, the averaged maximum nominal strain in BN of different thicknesses was quite close: 12.5 ± 3.0% for 1L BN and 13.3 ± 1.7% for 9L BN.

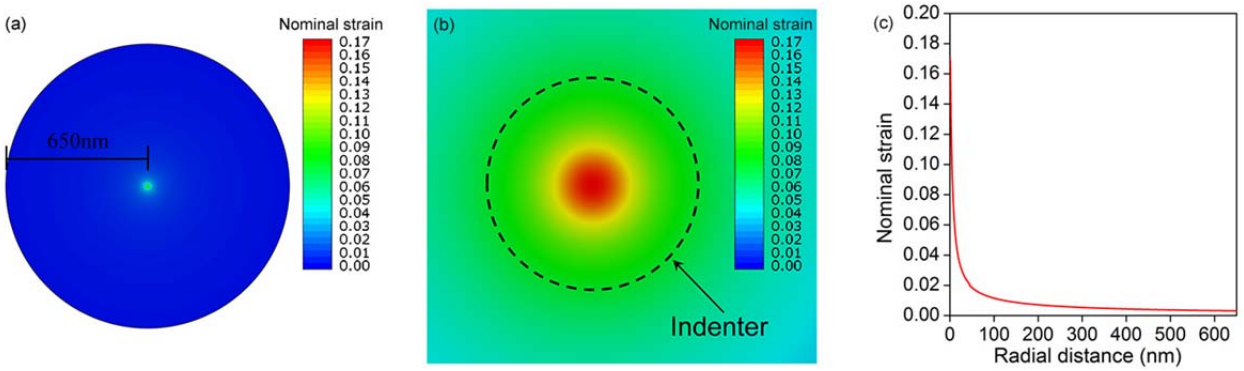

Figure 5. Strain distribution obtained from finite element simulations. (a) Nominal strain distribution in a 1L BN suspended over a micro-well with a radius of 650 nm under a fracture load; (b) enlarged view close to the indentation center, with the indenter tip (6.3 nm in radius) shown as a dashed circle; (c) strain distribution along the radius of the nanosheet under the fracture load.

Our results show that the strength of graphene largely decreased as the thickness increased. According to previous reports, this is due to interlayer slippage in few-layer graphene during indentation.[28] A similar phenomenon has also been observed from MoS_2/graphene and MoS_2/WS_2 heterostructures: the 2D Young's modulus and strength of heterostructures were smaller than the sum of those from each component.[36] However, the strength of the BN nanosheets remained constant over different thicknesses (Figure 4c). This difference between graphene and BN could be caused by different interlayer interactions in these nanomaterials despite of their analogous structure. We used *ab initio* density functional theory (DFT) calculations, including van der Waals interactions, to study the sliding energy in bilayer graphene and BN. According to the finite element simulations (Figure 5), most of the suspended

nanosheets (not close to the indentation center) experienced a very small in-plane strain and no out-of-plane compression even under the fracture load. The sliding energy in standard or equilibrium 2L graphene and BN can thus represent the interlayer interaction in the low-strained parts of the nanosheets. However, the small portions of graphene and BN nanosheets close to the indentation center were under a large in-plane tensile strain and out-of-plane compression, and there has been no study on how strain and compression affect their interlayer sliding. Figure 6a shows the finite element calculated strain distribution (solid lines) and out-of-plane pressure (dashed lines) in 2L graphene and BN within a radial distance of 10 nm from the indentation center under their fracture loads. In the vdW-corrected DFT calculations, we chose four combinations of strain and pressure conditions to reveal the interlayer interactions close to the indentation center of 2L graphene and BN. The four conditions correspond to radial distances of 0, 2, 4, and 10 nm away from the indentation center (grey vertical dotted lines in Figure 6a), and the strain + pressure values are hence 21.7% + 16.9 GPa (at a radial distance of 0 nm or the indentation center), 16.8% + 17.9 GPa (2 nm), 12.4% + 8.3 GPa (4 nm), and 7.2% + 0 GPa (10 nm) for 2L graphene; and 14.5% + 14.1 GPa (0 nm), 12.4% + 14.2 GPa (2 nm), 9.8% + 5.3 GPa (4 nm), and 5.7% + 0 GPa (10 nm) for 2L BN, respectively.

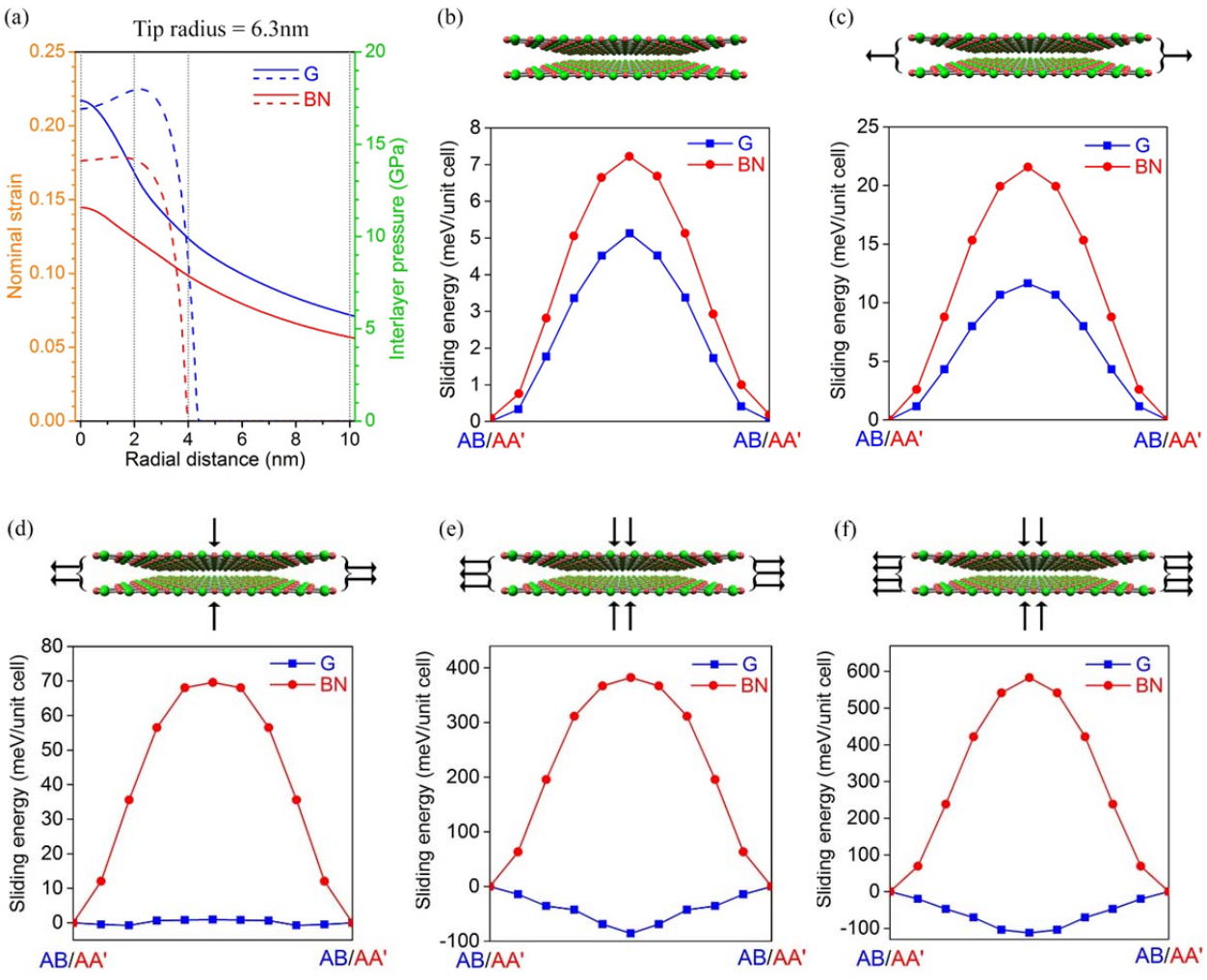

Figure 6. Changed sliding energies in 2L graphene and BN due to strain and pressure. (a) Finite element calculation induced in-plane strain (solid lines) and out-of-plane pressure (dashed lines) in 2L graphene and BN within a radial distance of 10 nm from the indentation center; (b-f) sliding energies in 2L graphene (AB to AB) and BN (AA' to AA') under five conditions: (b) equilibrium/standard state without strain or pressure, representing the portion of graphene and BN not close to the indentation center; (c) at a radial distance of 10 nm away from indentation center: 7.2% strain + 0 GPa pressure in 2L graphene, and 5.7% strain + 0 GPa pressure in 2L BN; (d) 4 nm away from indentation center: 12.4% strain + 8.3 GPa pressure in 2L graphene and 9.8% strain + 5.3 GPa pressure in 2L BN; (e) 2 nm away from indentation center: 16.8% strain + 17.9

GPa pressure in 2L graphene and 12.4% strain + 14.2 GPa pressure in 2L BN; (f) the indentation center or 0 nm: 21.7% strain + 16.9 GPa pressure in 2L graphene and 14.5% strain + 14.1 GPa pressure in 2L BN.

In standard or equilibrium crystal lattices (*i.e.* without strain or compression), the sliding energy from the AA' to AA' stacking in 2L BN was only slightly larger than that from the AB to AB stacking in 2L graphene, *i.e.* 7.22 *vs.* 5.12 meV per unit cell (Figure 6b). These results are consistent with previous calculations.[69,70] When 2L graphene and BN were strained without out-of-plane pressure (*i.e.* at a radial distance of 10 nm from indentation center, as shown in Figure 6a), both of their sliding energies increased: 11.64 meV for graphene, and 21.57 meV for BN (Figure 6c). Under further increased strain and pressure, 2L graphene and BN started to show a very different sliding tendency. At a radial distance of 4 nm, the sliding energy in 2L graphene reduced to almost zero, *i.e.* 0.92 meV/cell; while that in 2L BN further increased to 69.56 meV/cell (Figure 6d). Within a radial distance of 0-2 nm, the difference became more prominent: the sliding energy in graphene was as small as −112.26 meV/cell, but that in BN was as large as 582.84 meV/cell (Figure 6e and f). The rather different electronic characters of graphene and BN, *i.e.* semi-metallic and insulating, respectively, play a major role in their distinct sliding energies. When large strain and pressure are applied on graphene, its $2p_z$ orbitals tend to overlap; the more polar character of those orbitals in BN, on the other hand, localizes the electronic density. This difference results in opposite changes in sliding energy in the two materials under strain and pressure. These results indicate that the BN layers close to the indentation center were strongly glued and very unlikely to develop interlayer sliding. In striking contrast, the graphene layers could spontaneously slide between each other as the AB stacking was no longer stable.

We then used sandwich theory to quantitatively investigate how the different sliding energies in 2L graphene and BN could contribute to their different thickness-dependent mechanical properties. The two surface layers of 2L graphene and BN can be defined as faces, and the interlayer interactions including van der Waals interactions can be viewed as a core. Such designation meets the basic requirement for a sandwich structure where the faces are much stiffer than the core. In addition, the core in graphene and BN nanosheets satisfies the concept of an "antiplane" core, which has no contribution to the bending stiffness of the structure but can sustain a finite shear stress. During indentation, the sandwich structures of graphene and BN were simply-supported and subjected to central pointed loads. Given that there is no relative movement between the top and bottom faces under a central pointed load, the shear strain energy in the core (U_{shear}) of a sandwich structure can be described as:

$$U_{shear} = \frac{AG}{2}\int \gamma^2 \, dx \quad (6)$$

where γ is shear strain, which can be calculated by $\gamma = d/c \cdot dw_s/dx$ (d is the separation of the faces, and c is the thickness of the core); x is the distance to the central point of load; w_s is shear displacement, which is equal to $Fx/4AG$. F is the load, and AG is the shear stiffness of the sandwich structure (see Supplementary Information). The shear stiffness of graphene and BN was estimated based on the DFT-deduced sliding energy from the AB to AB stacking in graphene, and from the AA' to AA' stacking in BN. When no strain or compression was applied, the G values of graphene and BN were 4.99 and 6.78 GPa, respectively (see Supplementary Information). These values are in the range of previously reported values: 0.7−15.4 GPa for graphene/graphite,[71-75] and 2.5−9 GPa for BN.[54,76-78] However, under a large strain and

compression close to the indentation center, the G value of graphene became zero (*i.e.* spontaneous sliding), and that of BN increased enormously to 534 GPa. Therefore, the shear energy distributed over the radial distance of the suspended graphene and BN could be estimated (see Supplementary Information).

Figure 7a and c compare the shear strain energy (from the sandwich beam theory) and sliding energy (from the vdW-DFT simulations) in 2L graphene and BN at different radial distances from the indentation center under fracture loads. It is clear that the overall shear energy in graphene was much larger than the sliding energy, especially close to the indentation center (Figure 7a and b). Therefore, from the energetic point of view, the top layer of 2L graphene should slide towards the loading center during the indentation (Figure 7c). This would make the strain more concentrated on the bottom face of the 2L graphene, which is fixed onto the SiO_2 substrate. This explains why the fracture load and strength of 2L graphene are smaller than the two times of those of 1L graphene. On the other hand, the shear energy in 2L BN was always smaller than the sliding energy so that no slippage could occur (Figure 7d-f). This scenario resembled a sandwich beam with two fixed ends. According to the sandwich theory, such structure has no strain difference between the top and bottom faces. In other words, the strain is evenly distributed between the top and bottom faces. This justifies why the measured fracture load and strength of 2L BN were double those of 1L BN. As shown in Figure 8, BN nanosheets are one of the strongest electrically insulating materials.

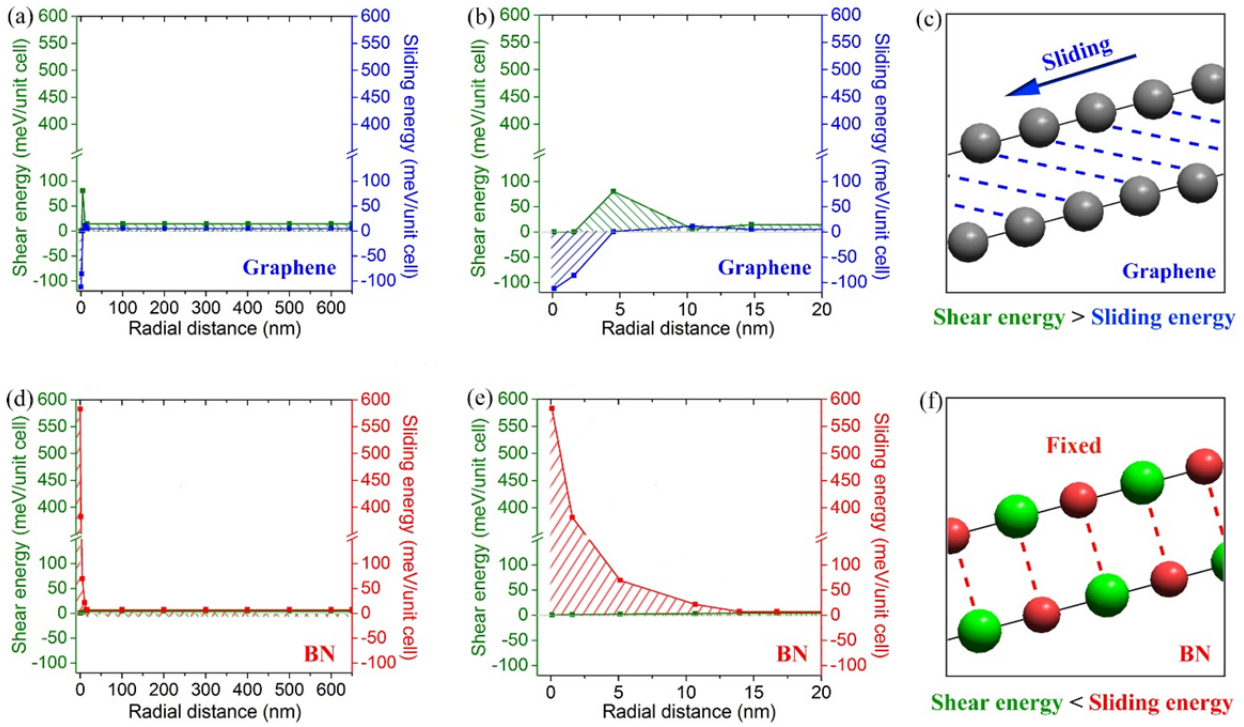

Figure 7. Slippage in graphene and fixed layers in BN. (a) Comparison between the shear energy and sliding energy in 2L graphene over a suspended radius of 650 nm under fracture load, as calculated by the sandwich beam theory and DFT simulation; (b) enlarged view of the region close to the indentation center; (c) diagram showing that the shear energy is larger than the sliding energy in graphene so that slippage happens spontaneously during indentation; (d) comparison between shear energy and sliding energy in 2L BN under a fracture load; (e) enlarged view of the region close to the indentation center; (f) diagram showing that the shear energy in 2L BN is smaller than the sliding energy so that no interlayer sliding can occur.

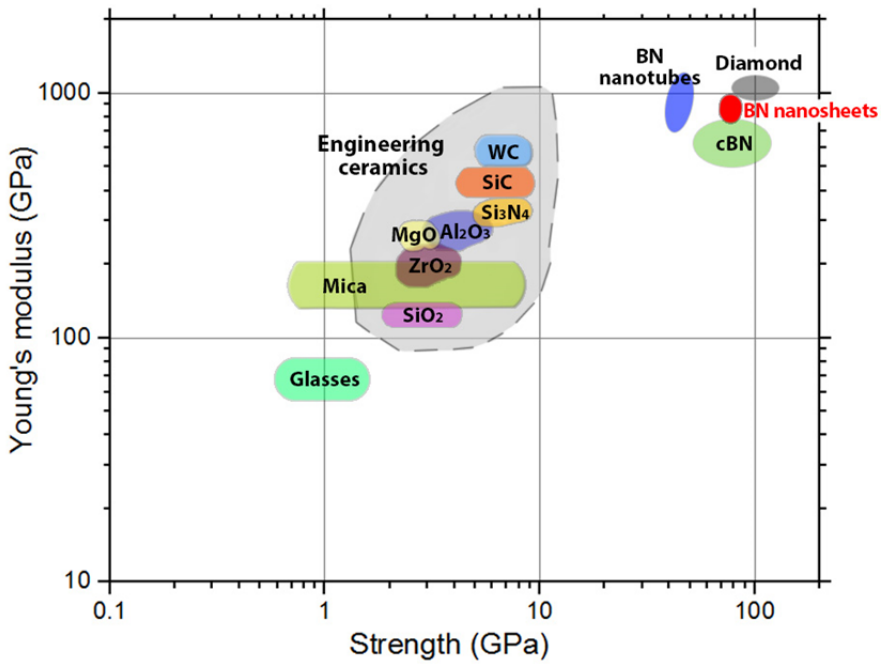

Figure 8. Modulus-strength graph comparing the mechanical properties of different electrically insulating materials, including monolayer and few-layer BN.

Discussion

We experimentally measured the mechanical properties of high-quality 1-9L BN nanosheets using AFM. Monolayer BN had a Young's modulus of 0.865 ± 0.073 TPa, and a fracture strength of 70.5 ± 5.5 GPa. Few-layer BN was as strong as 1L BN. This was very different to the case of graphene whose modulus and strength were found to decrease dramatically with increased thickness. Our DFT calculations including van der Waals interactions revealed that 2L graphene had negative sliding energies under an in-plane strain and large compression; while 2L BN could have enormous positive sliding energies under the same conditions. According to the sandwich beam theory, graphene layers tended to slide during indentation, but BN layers were strongly glued. Thus, the different trends in modulus and strength between graphene and BN

nanosheets with increasing thickness were caused by their dramatically different interlayer inteactions.

Methods

Materials and fabrication. Mechanical exfoliation by Scotch tape was used to prepare suspended graphene and BN nanosheets.[40,43,48] For comparison purposes, the indentation and fitting procedures for graphene and BN nanosheets were identical. A Cypher AFM was employed for the indentation tests. Two cantilevers with diamond tips were used because of the high strength of the membranes. The spring constants of the cantilevers were determined using a combination of the thermal noise method[79] and the Sader method.[80] The tip's radii were 5.6 and 6.3 nm, measured by transmission electron microscope (TEM). The indentation processes were conducted in ambient conditions and performed on relatively large nanosheets to prevent inaccuracy caused by their slippage on the substrate. The loading and unloading velocity for all measurements was constant (0.5 μm/s). Loading/unloading curves with no obvious hysteresis were used for fitting and calculations; curves showing large hystereses were excluded. The loading/unloading curves of few-layer graphene could not be reproduced by Eq. 1, and hence were fitted till ~50 nm of deflection for calculating the Young's moduli.

Finite element analysis. Computational simulations were performed using the commercial nonlinear finite element code ABAQUS. The diamond tips were modeled as rigid spheres. The nanosheets were modeled as axisymmetric membranes with a radius of 650 nm. The initial thicknesses for graphene and boron nitride nanosheets were assigned as $0.335\times N$ nm and $0.334\times N$ nm, respectively, where N is the number of layers. A total of 1663 two-node linear

axisymmetric membrane elements (MAX1) were employed with mesh densities varying linearly from 0.1 nm (center) to 1.0 nm (outermost). The interactions between the indenter tip and nanosheet were modeled by a frictionless contact algorithm. An indentation depth of 100 nm was applied to a prescribed displacement of 0.1 nm per load step. The constitutive behaviors of both graphene and BN were assumed to be nonlinear elastic, and thus expressed as:

$$\sigma = E\varepsilon + D\varepsilon^2 \qquad (7)$$

where E is Young's modulus and D is the third-order elastic constant. The Young's moduli of graphene and BN were set to 1000 GPa and 865 GPa, respectively. The value of D for graphene was −2000 GPa.[1] The value of D for BN was −2035 GPa, which was obtained from experimental results. The nonlinear elastic constitutive behavior was implemented in ABAQUS using an equivalent elastic-plastic material model as previously described.[1] To verify the nonlinear elastic effects, simulations using a linear elastic model were also performed by dropping the nonlinear term in Eq. 7 in the constitutive model. To compute the fracture strength, the load-displacement curves obtained from the finite element methods were compared with the corresponding experimental data, and the simulation loading steps corresponding to the point at which fracture took place were then identified based on the fracture loads from experiments. Subsequently, the fracture strength was obtained as a volume average of the stress values of the elements that were directly underneath the indenter at the corresponding loading steps. The interlayer pressure was approximated by the contact pressure between the indenter and nanosheets following the surface-to-surface contact model.[81]

van der Waals *ab initio* calculations. The calculations reported here are based on the *ab initio* density functional theory using the VASP code.[82,83] The generalized gradient approximation[84]

along with the opt-B88-vdW[85] functional was used, with a well-converged plane-wave cutoff of 1100 eV. Projected augmented wave method (PAW)[86,87] has been used in the description of the bonding environment for B, N, and C. The atomic coordinates were allowed to relax until the forces on the ions were less than 1×10^{-8} eV/Å under the conjugate gradient algorithm. The electronic convergence was set to 1×10^{-8} eV. The lattice constants for the monolayer BN unit cell were optimized and found to be a = 2.510 Å. To avoid any interactions between the supercells in the non-periodic direction, a 20 Å vacuum space was used in all calculations. The Brillouin zone was sampled with a 24 × 24 × 1 grid under the Monkhorst-Pack scheme[88] to perform relaxations with and without van der Waals interactions. In addition to this, we used a Fermi-Dirac distribution with an electronic temperature of k_BT = 20 meV to resolve the electronic structure.

References

1. Lee, C., Wei, X., Kysar, J. W. & Hone, J. Measurement of the elastic properties and intrinsic strength of monolayer graphene. *Science* **321**, 385-388 (2008).

2. Floriano, T., et al. Elastic properties of graphene suspended on a polymer substrate by e-beam exposure. *New J. Phys.* **12**, 023034 (2010).

3. Lee, J.-U., Yoon, D. & Cheong, H. Estimation of Young's modulus of graphene by Raman spectroscopy. *Nano Lett.* **12**, 4444-4448 (2012).

4. Frank, I. W., Tanenbaum, D. M., van der Zande, A. M. & McEuen, P. L. Mechanical properties of suspended graphene sheets. *J. Vac. Sci. Technol., B* **25**, 2558-2561 (2007).

5. Koenig, S. P., Boddeti, N. G., Dunn, M. L. & Bunch, J. S. Ultrastrong adhesion of graphene membranes. *Nat. Nanotechnol.* **6**, 543-546 (2011).

6. Philipp, W., Viktoria, V. I., Mark, J. R., Patrick, R. B. & Christopher, P. E. Mechanical properties of nanosheets and nanotubes investigated using a new geometry independent volume definition. *J. Phys. Condens. Matter* **25**, 155302 (2013).

7. Wei, X., Fragneaud, B., Marianetti, C. & Kysar, J. Nonlinear elastic behavior of graphene: *ab initio* calculations to continuum description. *Phys. Rev. B* **80**, 205407 (2009).

8. Zhao, H., Min, K. & Aluru, N. R. Size and chirality dependent elastic properties of graphene nanoribbons under uniaxial tension. *Nano Lett.* **9**, 3012-3015 (2009).

9. Costescu, B. I. & Grater, F. Graphene mechanics: II. atomic stress distribution during indentation until rupture. *PCCP* **16**, 12582-12590 (2014).

10. Cao, G. Atomistic studies of mechanical properties of graphene. *Polymers* **6**, 2404-2432 (2014).

11. Lee, G. H., et al. High-strength chemical-vapor-deposited graphene and grain boundaries. *Science* **340**, 1073-1076 (2013).

12. Zandiatashbar, A., et al. Effect of defects on the intrinsic strength and stiffness of graphene. *Nat. Commun.* **5**, 3186 (2014).

13. Lopez-Polin, G., et al. Increasing the elastic modulus of graphene by controlled defect creation. *Nat. Phys.* **11**, 26-31 (2015).

14. Liu, K., et al. Self-passivation of defects: effects of high-energy particle irradiation on the elastic modulus of multilayer graphene. *Adv. Mater.* **27**, 6841-6847 (2015).

15. Gomez-Navarro, C., Burghard, M. & Kern, K. Elastic properties of chemically derived single graphene sheets. *Nano Lett.* **8**, 2045-2049 (2008).

16. Suk, J. W., Piner, R. D., An, J. & Ruoff, R. S. Mechanical properties of monolayer graphene oxide. *ACS Nano* **4**, 6557-6564 (2010).

17. Zhang, P., et al. Fracture toughness of graphene. *Nat. Commun.* **5**, 3782 (2014).

18. Santos, E. J. G., Riiikonen, S., Sanchez-Portal, D. & Ayuela, A. Magnetism of single vacancies in rippled graphene. *J. Phys. Chem. C* **116**, 7602-7606 (2012).

19. Shekhawat, A. & Ritchie, R. O. Toughness and strength of nanocrystalline graphene. *Nat. Commun.* **7**, 10546 (2016).

20. Rasool, H. I., Ophus, C., Klug, W. S., Zettl, A. & Gimzewski, J. K. Measurement of the intrinsic strength of crystalline and polycrystalline graphene. *Nat. Commun.* **4**, 2811 (2013).

21. Ruiz-Vargas, C. S., et al. Softened elastic response and unzipping in chemical vapor deposition graphene membranes. *Nano Lett.* **11**, 2259-2263 (2011).

22. Mortazavi, B. & Cuniberti, G. Atomistic modeling of mechanical properties of polycrystalline graphene. *Nanotechnology* **25**, 215704 (2014).

23. Lee, C., et al. Elastic and frictional properties of graphene. *Phys. Status Solidi B* **246**, 2562-2567 (2009).

24. Zhang, Y. & Pan, C. Measurements of mechanical properties and number of layers of graphene from nano-indentation. *Diamond Relat. Mater.* **24**, 1-5 (2012).

25. Neek-Amal, M. & Peeters, F. M. Nanoindentation of a circular sheet of bilayer graphene. *Phys. Rev. B* **81**, 235421 (2010).

26. Zhang, Y. Y. & Gu, Y. T. Mechanical properties of graphene: effects of layer number, temperature and isotope. *Comput. Mater. Sci.* **71**, 197-200 (2013).

27. Scarpa, F., Adhikari, S. & Chowdhury, R. The transverse elasticity of bilayer graphene. *Phys. Lett. A* **374**, 2053-2057 (2010).

28. Wei, X. D., et al. Recoverable slippage mechanism in multilayer graphene leads to repeatable energy dissipation. *ACS Nano* **10**, 1820-1828 (2016).

454 29. Scharfenberg, S., et al. Probing the mechanical properties of graphene using a corrugated
455 elastic substrate. *Appl. Phys. Lett.* **98**, 091908 (2011).
456 30. Lin, Q. Y., et al. Step-by-step fracture of two-layer stacked graphene membranes. *ACS Nano*
457 **8**, 10246-10251 (2014).
458 31. Behfar, K. & Naghdabadi, R. Nanoscale vibrational analysis of a multi-layered graphene
459 sheet embedded in an elastic medium. *Compos. Sci. Technol.* **65**, 1159-1164 (2005).
460 32. Sakhaee-Pour, A., Ahmadian, M. T. & Naghdabadi, R. Vibrational analysis of single-layered
461 graphene sheets. *Nanotechnology* **19**, 085702 (2008).
462 33. Grantab, R., Shenoy, V. B. & Ruoff, R. S. Anomalous strength characteristics of tilt grain
463 boundaries in graphene. *Science* **330**, 946-948 (2010).
464 34. Bertolazzi, S., Brivio, J. & Kis, A. Stretching and breaking of ultrathin MoS_2. *ACS Nano* **5**,
465 9703-9709 (2011).
466 35. Castellanos-Gomez, A., et al. Elastic properties of freely suspended MoS_2 nanosheets. *Adv.*
467 *Mater.* **24**, 772-775 (2012).
468 36. Liu, K., et al. Elastic properties of chemical-vapor-deposited monolayer MoS_2, WS_2, and
469 their bilayer heterostructures. *Nano Lett.* **14**, 5097-5103 (2014).
470 37. Tao, J., et al. Mechanical and electrical anisotropy of few-layer black phosphorus. *ACS Nano*
471 **9**, 11362-11370 (2015).
472 38. Li, L. H. & Chen, Y. Atomically thin boron nitride: unique properties and applications. *Adv.*
473 *Funct. Mater.* **26**, 2594-2608 (2016).
474 39. Dean, C. R., et al. Boron nitride substrates for high-quality graphene electronics. *Nat.*
475 *Nanotechnol.* **5**, 722-726 (2010).

476 40. Li, L. H., et al. Dielectric screening in atomically thin boron nitride nanosheets. *Nano Lett.*
477 **15**, 218-223 (2015).
478 41. Li, L. H., et al. Photoluminescence of boron nitride nanosheets exfoliated by ball milling.
479 *Appl. Phys. Lett.* **100**, 261108 (2012).
480 42. Li, L., et al. High-quality boron nitride nanoribbons: unzipping during nanotube synthesis.
481 *Angew. Chem. Int. Ed.* **52**, 4212-4216 (2013).
482 43. Li, L. H., Cervenka, J., Watanabe, K., Taniguchi, T. & Chen, Y. Strong oxidation resistance
483 of atomically thin boron nitride nanosheets. *ACS Nano* **8**, 1457-1462 (2014).
484 44. Liu, L., et al. Graphene oxidation: thickness-dependent etching and strong chemical doping.
485 *Nano Lett.* **8**, 1965-1970 (2008).
486 45. Liu, Z., et al. Ultrathin high-temperature oxidation-resistant coatings of hexagonal boron
487 nitride. *Nat. Commun.* **4**, 2541 (2013).
488 46. Li, L. H., Xing, T., Chen, Y. & Jones, R. Boron nitride nanosheets for metal protection. *Adv.*
489 *Mater. Interfaces* **1**, 1300132 (2014).
490 47. Lin, Y., Bunker, C. E., Fernando, K. S. & Connell, J. W. Aqueously dispersed silver
491 nanoparticle-decorated boron nitride nanosheets for reusable, thermal oxidation-resistant surface
492 enhanced Raman spectroscopy (SERS) devices. *ACS Appl. Mater. Interfaces* **4**, 1110-1117
493 (2012).
494 48. Cai, Q., et al. Boron nitride nanosheets as improved and reusable substrates for gold
495 nanoparticles enabled surface enhanced Raman spectroscopy. *PCCP* **17**, 7761-7766 (2015).
496 49. Dai, P., et al. Pollutant capturing SERS substrate: porous boron nitride microfibers with
497 uniform silver nanoparticle decoration. *Nanoscale* **7**, 18992-18997 (2015).

50. Cai, Q., et al. Boron nitride nanosheet-veiled gold nanoparticles for surface-enhanced Raman scattering. *ACS Appl. Mater. Interfaces* **8**, 15630-15636 (2016).

51. Cai, Q., et al. Boron nitride nanosheets improve sensitivity and reusability of surface enhanced Raman spectroscopy. *Angew. Chem. Int. Ed.* **55**, 8405-8409 (2016).

52. Song, L., et al. Large scale growth and characterization of atomic hexagonal boron nitride layers. *Nano Lett.* **10**, 3209-3215 (2010).

53. Tongwei, H., Ying, L. & Chengyuan, W. Effects of temperature and strain rate on the mechanical properties of hexagonal boron nitride nanosheets. *J. Phys. D: Appl. Phys.* **47**, 025303 (2014).

54. Bosak, A., et al. Elasticity of hexagonal boron nitride: inelastic x-ray scattering measurements. *Phys. Rev. B* **73**, 041402 (2006).

55. Peng, Q., Ji, W. & De, S. Mechanical properties of the hexagonal boron nitride monolayer: *ab initio* study. *Comput. Mater. Sci.* **56**, 11-17 (2012).

56. Mirnezhad, M., Ansari, R. & Rouhi, H. Mechanical properties of multilayer boron nitride with different stacking orders. *Superlattices Microstruct.* **53**, 223-231 (2013).

57. Wu, J., Wang, B., Wei, Y., Yang, R. & Dresselhaus, M. Mechanics and mechanically tunable band gap in single-layer hexagonal boron-nitride. *Mater. Res. Lett.* **1**, 200-206 (2013).

58. Thomas, S., Ajith, K. M. & Valsakumar, M. C. Directional anisotropy, finite size effect and elastic properties of hexagonal boron nitride. *J. Phys. Condens. Matter* **28**, 295302 (2016).

59. Mortazavi, B. & Rémond, Y. Investigation of tensile response and thermal conductivity of boron-nitride nanosheets using molecular dynamics simulations. *Physica E* **44**, 1846-1852 (2012).

520 60. Zhao, S. J. & Xue, J. M. Mechanical properties of hybrid graphene and hexagonal boron
521 nitride sheets as revealed by molecular dynamic simulations. *J. Phys. D: Appl. Phys.* **46**, 135303
522 (2013).
523 61. Ding, N., Wu, C. M. L. & Li, H. The effect of grain boundaries on the mechanical properties
524 and failure behavior of hexagonal boron nitride sheets. *PCCP* **16**, 23716-23722 (2014).
525 62. Mortazavi, B. & Cuniberti, G. Mechanical properties of polycrystalline boron-nitride
526 nanosheets. *RSC Adv.* **4**, 19137-19143 (2014).
527 63. Kim, S. M., et al. Synthesis of large-area multilayer hexagonal boron nitride for high material
528 performance. *Nat. Commun.* **6**, 8662 (2015).
529 64. Li, C., Bando, Y., Zhi, C. Y., Huang, Y. & Golberg, D. Thickness-dependent bending
530 modulus of hexagonal boron nitride nanosheets. *Nanotechnology* **20**, 385707 (2009).
531 65. Taniguchi, T. & Watanabe, K. Synthesis of high-purity boron nitride single crystals under
532 high pressure by using Ba-BN solvent. *J. Cryst. Growth* **303**, 525-529 (2007).
533 66. Castellanos-Gomez, A., et al. Mechanical properties of freely suspended semiconducting
534 graphene-like layers based on MoS_2. *Nanoscale Res. Lett.* **7**, 233 (2012).
535 67. Al-Jishi, R. & Dresselhaus, G. Lattice-dynamical model for graphite. *Phys. Rev. B* **26**, 4514-
536 4522 (1982).
537 68. Kudin, K. N., Scuseria, G. E. & Yakobson, B. I. C_2F, BN, and C nanoshell elasticity from ab
538 initio computations. *Phys. Rev. B* **64**, 235406 (2001).
539 69. Gao, W. & Tkatchenko, A. Sliding mechanisms in multilayered hexagonal boron nitride and
540 graphene: the effects of directionality, thickness, and sliding constraints. *Phys. Rev. Lett.* **114**,
541 096101 (2015).

542 70. Marom, N., et al. Stacking and registry effects in layered materials: the case of hexagonal
543 boron nitride. *Phys. Rev. Lett.* **105**, 046801 (2010).
544 71. Blakslee, O. L., Proctor, D. G., Seldin, E. J., Spence, G. B. & Weng, T. Elastic constants of
545 compression‐annealed pyrolytic graphite. *J. Appl. Phys.* **41**, 3373-3382 (1970).
546 72. Mounet, N. & Marzari, N. First-principles determination of the structural, vibrational and
547 thermodynamic properties of diamond, graphite, and derivatives. *Phys. Rev. B* **71**, 205214
548 (2005).
549 73. Michel, K. H. & Verberck, B. Theory of the elastic constants of graphite and graphene. *Phys.*
550 *Status Solidi B* **245**, 2177-2180 (2008).
551 74. Zhang, Y. Y., Wang, C. M., Cheng, Y. & Xiang, Y. Mechanical properties of bilayer
552 graphene sheets coupled by sp^3 bonding. *Carbon* **49**, 4511-4517 (2011).
553 75. Hajgato, B., et al. Out-of-plane shear and out-of plane Young's modulus of double-layer
554 graphene. *Chem. Phys. Lett.* **564**, 37-40 (2013).
555 76. Green, J. F., Bolland, T. K. & Bolland, J. W. Theoretical elastic behavior for hexagonal
556 boron-nitride. *J. Chem. Phys.* **64**, 656-662 (1976).
557 77. Hamdi, I. & Meskini, N. *Ab initio* study of the structural, elastic, vibrational and
558 thermodynamic properties of the hexagonal boron nitride: Performance of LDA and GGA.
559 *Physica B* **405**, 2785-2794 (2010).
560 78. Lebedev, A. V., Lebedeva, I. V., Knizhnik, A. A. & Popov, A. M. Interlayer interaction and
561 related properties of bilayer hexagonal boron nitride: ab initio study. *RSC Adv.* **6**, 6423-6435
562 (2016).
563 79. Hutter, J. L. & Bechhoefer, J. Calibration of atomic‐force microscope tips. *Rev. Sci.*
564 *Instrum.* **64**, 1868-1873 (1993).

80. Sader, J. E., Chon, J. W. M. & Mulvaney, P. Calibration of rectangular atomic force microscope cantilevers. *Rev. Sci. Instrum.* **70**, 3967-3969 (1999).

81. Abaqus analysis user's guide 6.14.

82. Kresse, G. & Hafner, J. *Ab-initio* molecular-dynamics for open-shell transition-metals. *Phys. Rev. B* **48**, 13115-13118 (1993).

83. Kresse, G. & Furthmuller, J. Efficient iterative schemes for *ab initio* total-energy calculations using a plane-wave basis set. *Phys. Rev. B* **54**, 11169-11186 (1996).

84. Perdew, J. P., Burke, K. & Ernzerhof, M. Generalized gradient approximation made simple. *Phys. Rev. Lett.* **77**, 3865-3868 (1996).

85. Klimes, J., Bowler, D. R. & Michaelides, A. Chemical accuracy for the van der Waals density functional. *J. Phys. Condens. Matter* **22**, 022201 (2010).

86. Blochl, P. E. Projector augmented-wave method. *Phys. Rev. B* **50**, 17953-17979 (1994).

87. Kresse, G. & Joubert, D. From ultrasoft pseudopotentials to the projector augmented-wave method. *Phys. Rev. B* **59**, 1758-1775 (1999).

88. Monkhorst, H. J. & Pack, J. D. Special points for Brillouin-zone integrations. *Phys. Rev. B* **13**, 5188-5192 (1976).

Acknowledgements

L.H.Li thanks the financial support from Australian Research Council (ARC) via Discovery Early Career Researcher Award (DE160100796). A.Falin thanks Discovery Project (DP150102346) for scholarship. NSFC No.51420105002 and RSR by the Institute for Basic Science (IBS-R019- D1) are also acknowledged. E.J.G.Santos acknowledges the use of computational resources from the UK national high-performance computing service, ARCHER,

588 for which access was obtained via the UKCP consortium and funded by EPSRC grant ref
589 EP/K013564/1; and the Extreme Science and Engineering Discovery Environment (XSEDE),
590 supported by NSF grants TG-DMR120049 and TG-DMR150017. The Queens Fellow Award
591 through the start-up grant number M8407MPH and the Sustainable Energy PRP are also
592 acknowledged. D.Scullion thanks his EPSRC studentship. K.Watanabe and T.Taniguchi
593 acknowledge support from the Elemental Strategy Initiative conducted by the MEXT, Japan and
594 JSPS KAKENHI Grant Numbers JP26248061, JP15K21722 and JP25106006. Dr. Abu Sadek
595 assisted the fabrication of the percolated Si wafer at the Melbourne Centre for Nanofabrication
596 (MCN) in the Victorian Node of the Australian National Fabrication Facility (ANFF).
597

598 **Author contributions**

599 L.H.Li conceived and directed the project. A.Falin, Q.Cai and L.H.Li prepared the samples.
600 A.Falin performed indentation and analysed the data. E.J.G.Santos and D.Scullion did DFT
601 calculations. D.Qian and R.Zhang did finite element simulations. K.Watanabe and T.Taniguchi
602 provided hBN single crystals. R.Ruoff, Z.Yang and S.Huang discussed the results. Y.Chen and
603 M.R.Barnett reviewed the progress periodically. L.H.Li and A.Falin co-wrote the manuscript
604 with input from all authors.
605

606 **Additional information**

607 **Supplementary Information** accompanies this paper at http://www.nature.com/
608 naturecommunications
609 **Competing financial interests:** The authors declare no competing financial interests.
610